Reactive control of wave energy devices – the modelling paradox

Christian Windt [*,a,b], Nicolás Faedo [a], Markel Penalba [c], Frederic Dias [d], John V. Ringwood [a]

[a] Centre for Ocean Energy Research, Maynooth University, Co. Kildare, Ireland
[b] Leichtweiß–Institute for Hydraulic Engineering and Water Resources, Technische Universität Braunschweig, 38106 Braunschweig, Germany
[c] Mechanical and Industrial Production Department, Faculty of Engineering, Mondragon Unibertsitatea, Mondragon, Spain
[d] School of Mathematics and Statistics, University College Dublin, Dublin, Ireland

ARTICLE INFO

ABSTRACT

The implementation of energy maximising control systems (EMCSs) in wave energy converter (WEC) devices is an important step towards commercially viable operation of WECs. During the design stage of such EMCSs, linear hydrodynamic models are commonly used and are, in fact, the most viable option due to the real–time computational requirements of optimisation routines associated with energy-maximising optimal control techniques. However, the objective function of EMCSs, *i.e.* maximising the generated power by exaggerating WEC motion, inherently violates the underlying assumption of the linear hydrodynamic control design models, *i.e.* small amplitude device motion (compared to the device dimensions). Consequently, the linear models, used as a basis for EMCSs, in fact conspire to violate the very assumption upon which they were built - hence leading to a modelling paradox. It is important to evaluate WEC controllers in realistic physical or numerical environments, to gain knowledge of the disparity between the performance prediction from the EMCS design and performance evaluation models. This paper presents a comprehensive assessment of the performance prediction by a linear and non–linear hydrodynamic model of three different EMCSs, implemented in two different WEC structures, in an attempt to quantify the severity of this modelling disparity, or paradox.

1. Introduction

The widespread recognition of human–induced climate change and global warming has, in recent years, fuelled research and development (R&D) into novel technologies to harness renewable energy sources. Amongst these novel technologies, ocean wave energy converters (WECs) attract significant attention; however, device development is still in its infancy and current technologies are far from being commercially viable. To push WECs towards commercial viability, allowing the conversion of energy at a competitive levelised cost of energy (LCoE), energy maximising control systems (EMCSs) for WECs are under development (Ringwood et al., 2014). Since the objective of WEC control is to 'drive' the system towards resonance with the incoming wave field, the operational space of the WEC is enhanced (see Fig. 1), and, if performed correctly, power conversion is optimised.

During the design and evaluation of EMCSs, control engineers rely on numerical modelling, typically based on linear hydrodynamic models, either stemming from linear potential flow theory or data-driven system identification techniques (see Faedo et al. (2017) for further detail on dynamical models considered in the WEC control literature). Such linear models generally assume small wave amplitudes (relative to the wave length) and body motion (relative to the body dimensions). In classical control applications, the mathematical models, used for control design, are often linearised around a desired operational point, according to the process under analysis. The controller is subsequently synthesised to drive the system towards this set point and, thus, in the neighbourhood of this operational point, the linearising assumption is inherently obeyed.

However, the large amplitude motions, induced by a reactive WEC control action, may result in viscous drag, flow separation, vortex shedding, and other non-linear hydrodynamic effects (Penalba and Ringwood, 2019). Thus, in contrast to the aforementioned classical control applications, energy-maximising operating conditions and objectives do not comply with the linearising assumptions in the control design model. The contradiction between the control objective and the underlying mathematical model raises the question if the common practice of designing a controller in a linear design environment can deliver optimal reactive controllers for the application in physical, non-linear operational conditions. This is the essence of the WEC modelling paradox.

* Corresponding author.
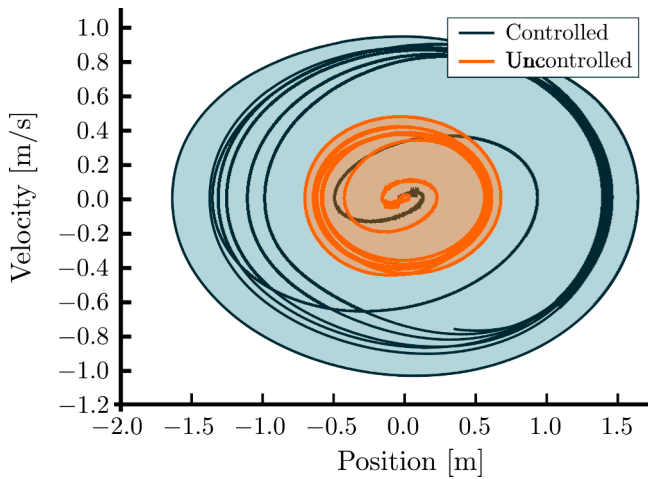 *E-mail address:* christian.windt.2017@mumail.ie (C. Windt).

Fig. 1. Operational (*phase*) space of an uncontrolled and controlled WEC device, with zero initial conditions and in regular waves: The velocity of the WEC in the heave direction is plotted over the WEC displacement in the heave direction (adapted from (Windt et al., 2019a)).

High–fidelity, computational fluid dynamics (CFD)–based numerical wave tanks (NWTs) (Kim et al., 1999, 2016; Tanizawa and Naito, 1997) have proven to be useful tools in WEC research and development (Wei et al., 2015; Windt et al., 2018a). Inherently capturing all relevant hydrodynamic non–linearities, these virtual test–beds are particularly valuable for the realistic evaluation of EMCSs for WEC applications, allowing investigation of the contradiction between the control design model assumptions and the resulting operational conditions.

1.1. Related studies

Giorgi and Ringwood (2016) describe the implementation of latching control for a generic, sphere–shaped WEC, in a CFD–based NWT which is used to evaluate optimal latching control parameters for a heaving point absorber in regular waves. The authors compare CFD–based results of the converted energy to results from a linear model, where the latter is based on boundary element method (BEM)–based potential flow solutions. The presented results highlight differences in the optimal control parameters and, ultimately, in an over––prediction in converted energy by the BEM–based linear model.

Also considering a generic, sphere–shaped WEC, Davidson et al. (2017) implement a reactive feedback controller in a CFD–based NWT, where the control parameters (stiffness and damping coefficients) are determined from data-based models (Davidson et al., 2015, 2016), as well as BEM–based potential flow solutions. As in Giorgi and Ringwood (2016), comparing the CFD–based NWT results against linear potential flow simulations shows that the linear simulations overestimate the WEC motion and power absorption.

A more complex, adaptive, EMCS, based on a receding-horizon pseudospectral optimal control (RHPC) formulation, is implemented and evaluated in a CFD–based NWT by Davidson et al. (2018). Online system identification methods are employed in the control algorithm to identify and update the linear control model during the simulation, creating a best fitting linear control model representative of the non-linear conditions in the CFD–based NWT. A direct comparison between the non–linear, CFD–based NWT and the linear modelling framework is only undertaken for the parameter adaption of the adaptive RHPC. The comparison shows unsurprising larger changes of the controller parameters within the CFD–based modelling framework, which the authors justify by e.g. viscous damping, present in the CFD–based NWT.

1.2. Objectives

Motivated by the fact that the vast majority of WEC controllers are designed based on linear hydrodynamic design models, which are representative under uncontrolled conditions (*i.e.* in the region delimited using orange in Fig. 1), this paper extends the existing literature by assessing the reliability of linear EMCS design models for power production estimation. This is achieved by evaluating the performance of three different EMCSs, designed with a linear design model stemming from data–driven system identification (Bacelli et al., 2017), in both a linear and non-linear hydrodynamic modelling framework. The different EMCSs, considered in this study, are as follows: Resistive (*i.e.* velocity feedback only) controller, reactive (*i.e.* displacement and velocity feedback) controller, and the recently published energy-maximising moment-based controller by Faedo et al. (2018c, 2019). These control strategies, which are described in detail in Section 3.2, show varying levels of aggressiveness in terms of control action.

The non–linear hydrodynamic model in the evaluation stage is based on a CFD–based NWT, while the linear hydrodynamic model in the evaluation stage is the same as the model used during the design stage. For this study, two different moored, heaving, point absorber–type WEC structures are considered.

Based on this comprehensive case study, the paper aims to answer the question if, due to the contradiction between the EMCS design model and the resulting operational conditions, linear reactive controllers for WECs are inherently limited in addressing the WEC modelling paradox.

1.3. Paper outline

The remainder of this paper is organised as follows. Section 1.4 details any non-standard notation used throughout this study. Section 2 provides the details of the considered case study, in particular the WEC structures and the incident sea state. Section 3 presents the system identification methodology, used to determine the linear, hydrodynamic, control design model, as well as the details of the WEC controllers and their synthesis. Section 4 introduces the test cases considered during this study, which can be divided into system identification and control design, validation, and evaluation. Section 5 presents the details of the CFD–based NWT. Results for the different test cases are shown and discussed in Section 6. Finally, conclusions are drawn in Section 7.

1.4. Notation

Standard notation is used throughout this study with any exception detailed in this section. $\mathbb{R}^+$ ($\mathbb{R}^-$) denotes the set of non-negative (non-positive) real numbers. $\mathbb{C}^0$ denotes the set of pure-imaginary complex numbers, while $\mathbb{C}_{<0}$ denotes the set of complex numbers with (strictly) negative real part. The symbol 0 stands for any zero element, dimensioned according to the context. The notation $\mathbb{N}_q$ indicates the set of all positive natural numbers up to q, *i.e.* $\mathbb{N}_q = \{1, 2, \cdots, q\}$. The symbol $\mathbb{I}_n$ denotes the identity matrix of the Euclidean space $\mathbb{C}^{n \times n}$. The spectrum of a matrix $A \in \mathbb{R}^{n \times n}$, *i.e.* the set of its eigenvalues, is denoted as $\lambda(A)$. The symbol $\bigoplus$ denotes the direct sum of n matrices, *i.e.* $\bigoplus_{i=1}^n A_i = \text{diag}(A_1, A_2, \cdots, A_n)$. The *Kronecker product* between two matrices $M_1 \in \mathbb{R}^{n \times m}$ and $M_2 \in \mathbb{R}^{p \times q}$ is denoted by $M_1 \otimes M_2 \in \mathbb{R}^{np \times mq}$. The *Kronecker sum*[1] between two matrices P_1 and P_2, with $P_1 \in \mathbb{R}^{n \times n}$ and $P_2 \in \mathbb{R}^{k \times k}$, is denoted as $P_1 \widehat{\oplus} P_2$. Finally, the symbol $\varnothing$ denotes the empty set.

2. Case study

This section introduces the WEC structures and incident sea state considered throughout this study.

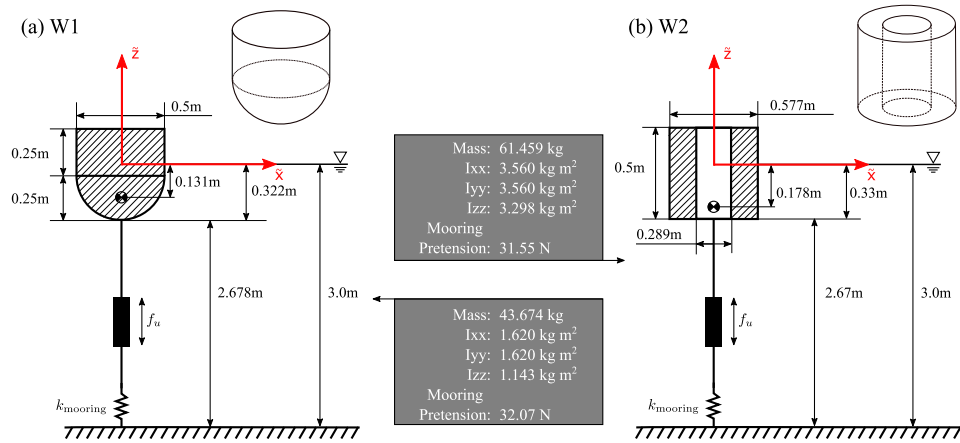[1] See Brewer (1978) for a formal definition of the Kronecker sum operator.

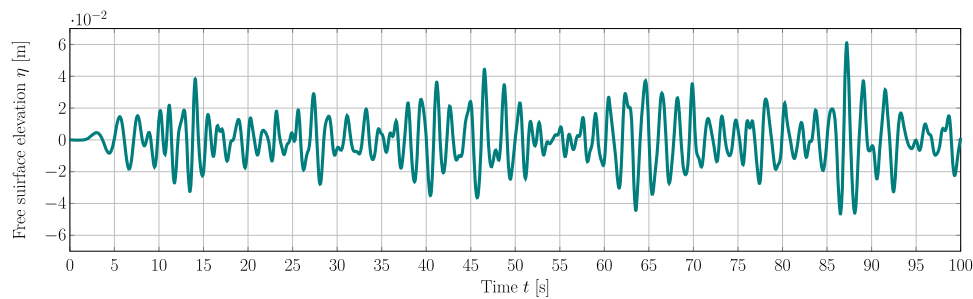**Fig. 2.** Schematic of the considered WEC structures: W1 (a) and W2 (b).

Fig. 3. Time trace of the incident, irregular wave measured in the CFD–based NWT at the intended WEC location.

2.1. WEC Structures

Two different WEC structures are considered, W1 and W2, resembling moored, point absorber–type devices with axisymmetric, cylindrical, geometries. The WECs are based on the systems considered for the Blind Test Series 2 and 3 of the Collaborative Computational Project in Wave Structure Interaction and have been extensively analysed experimentally and numerically (Ransley et al., 2020a, 2020b). In contrast to the experimental setup documented in (Ransley et al., 2020a, 2020b), for this study device motion is constrained to a single degree of freedom, i.e. heave.

Schematics of the two structures including all relevant physical properties are shown in Figs. 2 (a) and (b). While W1 features a hemispherical bottom, W2 features a sharp-cornered bottom and a moonpool. The mooring of the structures is implemented via a linear spring, with a stiffness of $k_{\mathrm{mooring}} = 67 Nm^{-1}$, connecting the device with the tank floor. Characteristic frequencies of the structures W1 and W2 are $5.85 rads^{-1}$ and $[4.33 rads^{-1}\ 5.22 rads^{-1}]$, respectively, as will be shown in Section 6.1. In Fig. 2, $f_{\mathrm{u}} : \mathbb{R}^+ \to \mathbb{R}, t \mapsto f_{\mathrm{u}}(t)$, indicates the control force (see Section 3). In this study, the device motion is constrained to heave only, thus, the displacement and velocity of the devices are denoted as $z : \mathbb{R}^+ \to \mathbb{R}, t \mapsto z(t)$, and $\dot{z} : \mathbb{R}^+ \to \mathbb{R}, t \mapsto \dot{z}(t)$, respectively.

2.2. Incident sea state

In this study, an irregular, JONSWAP sea state with a significant wave height of $H_s = 0.1m$ and a peak period of $T_p = 1.94s$ is considered, representing realistic, scaled, conditions at the AMETS test site in Bellmullet, Co. Mayo, off the West Coast of Ireland (Sharkey et al., 2011).

For Blind Test Series 2 and 3, the WEC structures were tested in a physical wave tank with 3m water depth. Thus, Froude scaling with a scaling factor of $1/30$th (Heller, 2011) is applied, to retain deep water conditions of the AMETS site.

A time trace of the recorded free surface elevation, measured in the CFD–based NWT at the intended WEC location, during a preliminary wave-only simulation is shown in Fig. 3. Note that the presented time trace does not show a statistically converged JONSWAP spectrum. This would require relatively long time traces which are, due to the computational demand of CFD simulations, infeasible for the present study. However, this imperfection does not influence the presented results.

3. System identification and WEC control

As previously discussed in Section 1, the vast majority of WEC control strategies, proposed to optimise energy absorption from incoming waves, are *model-based*: a mathematical structure, *i.e.* a model Σ (commonly defined over a finite-dimensional space) describing the dynamics of the WEC system, is required to compute the corresponding energy-maximising control law. Naturally, there is a 'limit' to the complexity of these mathematical models for which an optimal energy-maximising control solution can be effectively found in *real-time*, either algebraically or numerically (see, for instance, Faedo et al. (2017); Penalba and Ringwood (2020)).

Motivated by the above requirements, *linear* WEC systems are virtually always used, reflecting both their simplicity and associated computational convenience. Such linear models are often written in terms of a state-space (parametric) representation, defined (at least locally) over a real-valued Euclidean space. A number of methods can be

used to obtain a WEC model Σ, ranging from the (pure) use of physical principles (*i.e. white-box* modelling), to determining a mathematical structure and parameters directly from input-output data (*i.e. black-box* modelling) (Ljung, 1999). In this paper, a mathematical model for each corresponding WEC system, W1 and W2, is computed following standard procedures of black-box modelling, *i.e.* using input-output *system identification* techniques (Ljung, 1999).

3.1. System identification

In this study, the linear control design model is obtained via 'classical' system identification techniques, following a frequency-domain black-box-identification methodology[2]. To be precise, the WEC structure, implemented in the CFD–based NWT, is driven by a finite-set of N *sufficiently exciting* (Ljung, 1999) input signals[3] $\mathscr{U} = \{f_i\}_{i=1}^{N}$, with $N \in \mathbb{N}_{\geq 1}$, generating a corresponding set of outputs $\mathscr{Y} = \{y_i\}_{i=1}^{N}$ (which in this case are heave velocities). Aiming to identify the so-called *force-to-velocity* mapping, *i.e.* the map $f_i \mapsto y_i$, each input force $f_i : \mathbb{R}^+ \to \mathbb{R}$ in the set $\mathscr{U}$ is chosen as an *up-chirp* signal (see, for instance, Ljung (1999)), with N different amplitudes contained in a set $\mathscr{A} \subset \mathbb{R}^+$. In line with the main objective of this paper, that is, to evaluate the performance of energy-maximising control techniques based on WEC models computed under linear uncontrolled conditions in realistic scenarios (i.e. within a high-fidelity CFD solver), the set of amplitudes $\mathscr{A}$ needs to be selected such that the input-output mapping $f_i \mapsto y_i$ can be reasonably represented in terms of a linear parametric structure. In other words, if $A_i \in \mathscr{A}$, then A_i needs to be sufficiently small, for all $i \in \mathbb{N}_N$.

Let (f_i, y_i) denote an input-output pair of signals for the WEC system. Following standard frequency-domain techniques, the so-called empirical transfer function estimate (ETFE) $H_i : \mathbb{C} \to \mathbb{C}$, $j\omega \mapsto H_i(j\omega)$, can be readily computed, for each input-output pair, using the expression

$$H_i(j\omega) = \frac{Y_i(j\omega)}{F_i(j\omega)}, \tag{1}$$

with $i \in \mathbb{N}_N$, and where $Y_i : \mathbb{C} \to \mathbb{C}$ and $F_i : \mathbb{C} \to \mathbb{C}$ denote the Fourier transform of y_i and f_i, respectively. Once the set $\{H_i\}_{i=1}^{N}$ is obtained, the average empirical transfer function estimate, $\overline{H}$, is computed, aiming to build a low-variance set, used as the input to the frequency-domain identification algorithm (Ljung, 1999). The explicit expression of $\overline{H}$ is simply given by:

$$\overline{H}(j\omega) = \frac{1}{N} \sum_{i=1}^{N} H_i(j\omega). \tag{2}$$

The ultimate objective of this system identification procedure is to obtain a parametric form approximating the behaviour of the WEC system under analysis, which, in this case, is characterised by the average ETFE (2), computed explicitly using the CFD-based NWT. The technique used to achieve such a parametric form is the *moment-matching-based* identification framework presented by Faedo et al. (2018a,b), which provides an approximation of $\overline{H}$ in terms of a state-space representation Σ. In particular Σ is a deterministic, finite-dimensional system, given, for $t \in \mathbb{R}^+$, by the set of differential equations,

$$\overline{H}(j\omega) \approx \Sigma : \begin{cases} \dot{x} = Ax + B(f_e - f_u), \\ y = Cx = \dot{z}, \end{cases} \tag{3}$$

where $x(t) \in \mathbb{R}^n$ is the *state-vector*, with the order of the system, n, $A \in \mathbb{R}^{n \times n}$, $\{B, C^\intercal\} \subset \mathbb{R}^n$, $f_e : \mathbb{R}^+ \to \mathbb{R}$ is the wave excitation force, and the output

$y = \dot{z}$, $\dot{z}(t) \in \mathbb{R}$, corresponds with the velocity of the WEC system. Note that the system identification technique presented by Faedo et al. (2018a,b), guarantees preservation of both internal stability (in the Lyapunov sense), *i.e.* $\lambda(A) \subset \mathbb{C}_{<0}$, and *passivity* (see, for instance, Khalil (1996)). The latter is an input-output property which stems from the underlying physical principles associated with the WEC, and is required to guarantee existence and uniqueness of a globally optimal solution for the moment-based energy-maximising controller (Faedo et al., 2018c, 2019) (presented in Section 3.3).

3.2. WEC Control

The main objective of a wave energy device is to harvest energy from the incoming wave field.[4] Therefore, the optimal control objective is to maximise the absorbed energy over a time in terval[5] $\mathscr{T} = [0, T] \subset \mathbb{R}^+$, written in terms of the objective function $E : \mathbb{R} \to \mathbb{R}$, $f_u \mapsto E(f_u)$,

$$E(f_u) = \frac{1}{T} \int_{\mathscr{T}} f_u(\tau) \dot{z}(\tau) \, d\tau = \frac{1}{T} \int_{\mathscr{T}} P(\tau) \, d\tau, \tag{4}$$

where P denotes the *instantaneous power*. Note that this energy-maximising control objective does not fit into a traditional (reference tracking) control problem, *i.e.* the performance objective is strictly related to the maximisation of energy absorption. Consequently, the energy-maximising control objective can be formulated in terms of an optimal control problem (OCP), *i.e.* find $f_u : \mathbb{R}^+ \to \mathbb{R}$, $t \mapsto f_u(t)$, such that

$$\begin{aligned} f_u^{\text{opt}} &= \underset{f_u}{\arg\max} E(f_u) \\ &\quad \text{subject to:} \\ &\quad \text{WEC dynamics given by} \Sigma in (3) \end{aligned} \tag{5}$$

Note that, though not considered in this paper, *state* and *input* constraints can also be directly incorporated to the OCP (5), as a set of inequalities in f_u (Faedo et al., 2017).

3.3. Moment-based optimal control

The moment-based energy-maximising control strategy presented by Faedo et al. (2018c, 2019) provides an efficient and convenient way to parameterise the input and state variables in terms of the *system-theoretic* concept of *moments* (see Astolfi (2010)). Moments are intrinsically connected to the steady-state response characteristics of the system (WEC) under analysis, allowing for a parameterisation of problem (5) in terms of the steady-state response of a suitably defined interconnected system.

In particular, given the harmonic nature of ocean waves, (Faedo et al., 2018c, 2019) the excitation force f_e and control input f_u are expressed as the solution of a *signal generator* $\mathscr{G}$ (also commonly known as *exogenous system* (Isidori, 2013)), described by the set of equations

$$\mathscr{G} : \begin{cases} \dot{\xi} &= S\xi, \\ f_e &= L_e \xi, \\ f_u &= L_u \xi, \end{cases} \tag{6}$$
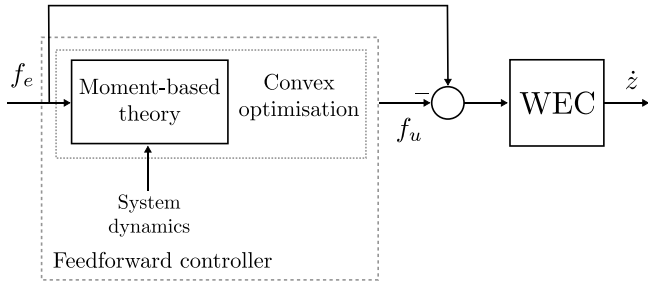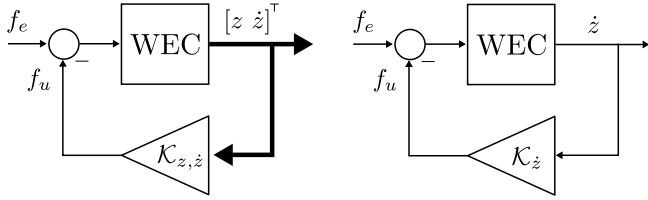

Fig. 4. Moment-based control structure.

Fig. 5. Reactive (left) and resistive (right) control structures.

where the dynamic matrix $S \in \mathbb{R}^{\nu \times \nu}$ is such that $\lambda(S) = \{ \pm jp\omega_0 \}_{p=1}^{\nu/2} \subset \mathbb{C}$, with ν integer and even, and where ω_0 is the so-called *fundamental frequency* associated with the input variables f_e and f_u, i.e. $\omega_0 = 2\pi / T$. With the parameterisation of Equation (6), and the state-space WEC system (3), the OCP (5) can be mapped into a quadratic program (QP), i.e. the energy-maximising control input $f_u^{\mathrm{opt}} = L_u^{\mathrm{opt}}\xi$ can be computed as the unique global solution of the *concave* quadratic optimisation problem

$$L_u^{\mathrm{opt}} = \arg\max_{L_u^\mathsf{T} \in \mathbb{R}^\nu} -\frac{1}{2}L_u\Psi^\mathsf{T}L_u^\mathsf{T} + \frac{1}{2}L_e\Psi^\mathsf{T}L_u^\mathsf{T}, \tag{7}$$

where the matrix $\Psi \in \mathbb{R}^{\nu \times \nu}$ explicitly characterises both the WEC dynamics, and the input description, as

$$\Psi = (\mathbb{I}_\nu \otimes C)(S \widehat{\oplus} A)^{-1}(\mathbb{I}_\nu \otimes -B). \tag{8}$$

Note that $0 \notin \lambda(S \widehat{\oplus} A)$, since $\lambda(A) \cap \lambda(S) = \varnothing$, and, hence, the inverse of $S \widehat{\oplus} A$ is always well-defined (Brewer, 1978). Fig. 4 shows a block-diagram of the *feedforward* control architecture associated with

(7).

3.4. Reactive and resistive feedback controllers

In addition to the moment-based controller, less 'aggressive' EMCSs, i.e. so-called *reactive* and *resistive* feedback controllers, are considered as reference cases. Both reactive and resistive strategies are varieties of 'traditional' output feedback WEC controllers (see, for instance, Khalil (1996)), as detailed in the following. For the reactive control case, the PTO force follows from an output feedback technique, involving both displacement and velocity of the WEC system, i.e.

$$f_u = K_1 z + B_1 \dot{z}, \tag{9}$$

where the matrix $\mathscr{K}_{z,\dot{z}} = [K_1 \ B_1]^\mathsf{T} \in \mathbb{R}^2$ is the optimal reactive feedback gain, i.e. such that it maximises (5) when the control solution is constrained to be of an output feedback type.

Similarly, for the resistive control case, the PTO force follows from an output feedback technique, but only involving the velocity of the WEC system, i.e.

$$f_u = B_2 \dot{z}, \tag{10}$$

where the scalar value $\mathscr{K}_{\dot{z}} = B_2 \in \mathbb{R}$ is the optimal resistive feedback gain.

Both optimal gains, i.e. $\mathscr{K}_{z,\dot{z}}$ and $\mathscr{K}_{\dot{z}}$, are commonly computed following exhaustive search procedures (see the procedure described by Windt et al. (2018b)), explicitly using the dynamical model obtained via system identification techniques, i.e. system Σ in Equation (3). A block-diagram of both reactive (right) and resistive (left) control strategies, is illustrated in Fig. 5.

4. Test cases

The present study is divided into three main steps, requiring specific sets of test cases. The steps are: System identification and control design, validation, and performance evaluation. The specific test cases are detailed in the following.

4.1. System identification and control design

Initially, system identification chirp test cases are simulated to provide the required data for the system identification procedure outlined
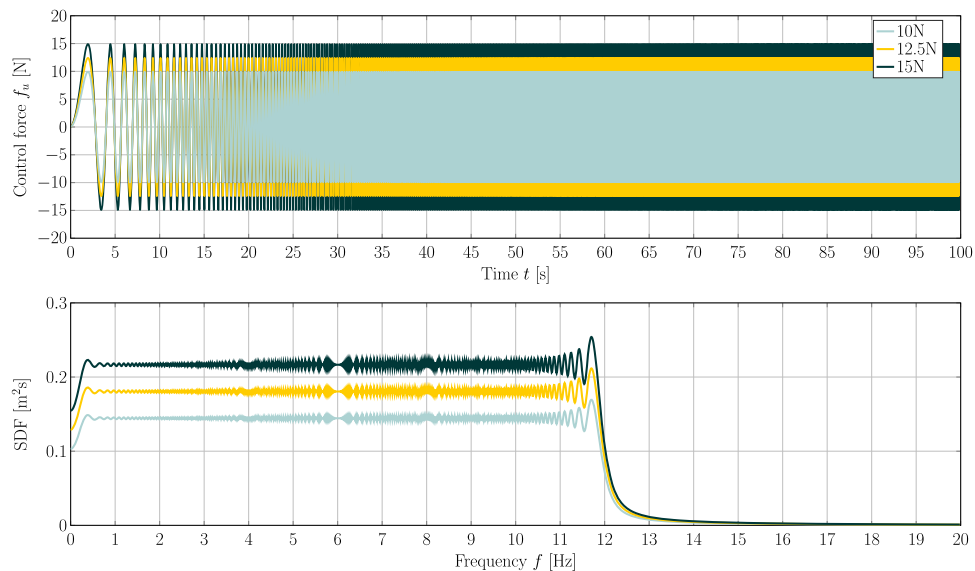

Fig. 6. Time traces and spectral density distributions of the control forces f_u for the multi–frequency forced oscillation.

in Section 3.1. Subsequently, wave excitation force tests are required to produce the required data for the control synthesis, outlined in Section 3.2.

4.1.1. Multi–frequency forced oscillation

For the up-chirp tests, each element f_i in the set of input forces $\mathscr{U}$ (see Section 3.1) is defined as a linear frequency sweep in the range $[0.1, 60.0]\,rads^{-1}$, with 3 different amplitudes, *i.e.* $N = 3$ in (2), contained in the set $\mathscr{A} = \{10.0\,N, 12.5\,N, 15.0\,N\}$ (see Fig. 6). Note that several force amplitudes are considered to cater for the computation of the average empirical transfer function estimate $\overline{H}$, aiming to build a low-variance set, used as the input to the frequency-domain identification algorithm.

Each of these forces is fed to the system through the motion solver of the CFD–based NWT (see Section 5). The input forces f_i, and the post––processed device motions y_i, are then directly used within the system identification procedure, described in Section 3.1. This is specifically addressed in Section 6, for each of the defined WEC structures (*i.e.* W1 and W2).

4.1.2. Wave excitation force tests

As stated in Section 3.2, with the identified linear WEC model, the three EMCSs can be synthesised under the assumption of perfect knowledge of the wave excitation force. To acquire the required wave excitation force signals for controller synthesis, wave excitation force tests are simulated, where the WEC structures are held fixed in their equilibrium position and are exposed to the incident sea state depicted in Fig. 3. The wave excitation force is extracted from the numerical data in a post–processing step.

4.2. Validation

To ensure and assess the quality of the identified linear WEC models, validation test cases are considered. The motion of the WEC structures, exposed to the irregular sea state, shown in Fig. 3, is simulated in the CFD–based and linear modelling framework under uncontrolled conditions. In such conditions, the two models (identified, representative, linear and CFD–based) are expected to deliver similar results, thereby ensuring a fair comparison during the controller evaluation step.

4.3. Performance evaluation

Finally, in the performance evaluation step, the motion of the WEC structures, exposed to the irregular sea state, is simulated in the CFD–based and linear modelling framework under controlled conditions, using the three different EMCSs detailed in Section 3.2. Comparing time traces of the WEC motion and control force, as well as absorbed energy, allows a comprehensive evaluation of the controller performance, predicted in both the linear and CFD–based modelling frameworks. It should be noted that the irregular sea state is the same in both the validation and performance evaluation stage. With this choice, potential modelling errors can be omitted. Knowing that the identified model validates well against the CFD model for a given irregular wave train and, subsequently, using the exact same wave train together with EMCSs, associates the observed differences with the non-linearities, induced by the action of the EMCS.

5. Numerical wave tank

The CFD–based NWT is implemented using the open-source CFD toolbox OpenFOAM, version 1812. In this section, the CFD–based NWT setup, adapted from Windt et al. (2019a) and validated by Windt et al. (2020b,c), is detailed. The governing equations are presented (see
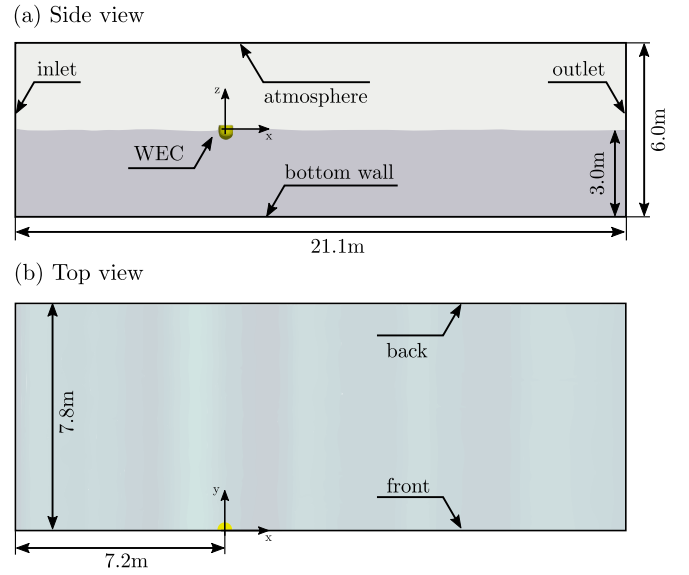

(a) Side view

(b) Top view

Fig. 7. Schematic of the numerical wave tank: Side view (a) and top view (b).

Section 5.1), as well as the treatment of numerical wave generation and absorption (see Section 5.2), and the specifics of the computational domain (see Section 5.3).

5.1. Governing equations

The hydrodynamics in the CFD–based NWT are modelled by solving the incompressible Reynold Averaged Navier-Stokes (RANS) equations, describing the conservation of mass and momentum. The conservation equations for mass and momentum in differential form are shown in Equations (11) and (12), respectively.

$$\frac{\partial \rho(t,\mathbf{x})}{\partial t} + \nabla\cdot(\rho(t,\mathbf{x})\mathbf{U}(t,\mathbf{x})) = 0 \tag{11}$$

$$\frac{\partial \rho(t,\mathbf{x})\mathbf{U}(t,\mathbf{x})}{\partial t} + \nabla\cdot\rho\mathbf{U}(t,\mathbf{x})\mathbf{U}(t,\mathbf{x}) = -\nabla p(t,\mathbf{x}) + \nabla\cdot(\mu\nabla\mathbf{U}(t,\mathbf{x})) + \rho\mathbf{f}_b(t,\mathbf{x})$$
$$+ \mathbf{f}_u(t,\mathbf{x}) \tag{12}$$

In Equations (11) and (12), t denotes time, $\mathbf{U}(t)$ is the fluid velocity field, $p(t)$ the fluid pressure, ρ the fluid density, μ the dynamic viscosity, and $\mathbf{f}_b(t)$ the external forces, such as gravity. To account for the two phase flow, the volume of fluid (VoF) method, proposed by Hirt and Nichols (1981), is employed. Defining a volume fraction, α, the properties of the fluid mixture (density and viscosity) can be expressed as:

$$\rho(t,\mathbf{x}) = \alpha(t,\mathbf{x})\rho_{\text{water}}(t,\mathbf{x}) + (1 - \alpha(t,\mathbf{x}))\rho_{\text{air}}(t,\mathbf{x}), \tag{13}$$

and

$$\mu(t,\mathbf{x}) = \alpha(t,\mathbf{x})\mu_{\text{water}}(t,\mathbf{x}) + (1 - \alpha(t,\mathbf{x}))\mu_{\text{air}}(t,\mathbf{x}). \tag{14}$$

In OpenFOAM, the transport equation for α follows:

$$\frac{\partial \alpha(t,\mathbf{x})}{\partial t} + \nabla\cdot(\mathbf{U}(t,\mathbf{x})\alpha(t,\mathbf{x})) + \nabla\cdot[\mathbf{U}_r(t,\mathbf{x})\alpha(t,\mathbf{x})(1 - \alpha(t,\mathbf{x}))] = 0, \tag{15}$$

where $\mathbf{U}_r(t)$ is the relative velocity between the liquid and gaseous phases (Berberović et al., 2009). Boundedness of the transport equation is achieved through the multi-dimensional limiter for explicit solutions

Table 1

OpenFOAM boundary conditions in the computational domain with the initial conditions in brackets; The asterisk marks IHFOAM specific boundary conditions.

	U		p_rgh		point displacement		α	
back	fixed Value	(0 0 0)	fixedFluxPressure	(0)	fixed Value	(0 0 0)	zeroGradient	(0)
front	symmetry		symmetry		symmetry		symmetry	
bottom wall	fixed Value	(0 0 0)	fixedFluxPressure	(0)	fixed Value	(0 0 0)	zeroGradient	(0)
inlet	waveVelocity*	(0 0 0)	fixedFluxPressure	(0)	fixed Value	(0 0 0)	waveAlpha*	
outlet	waveVelocity*	(0 0 0)	fixedFluxPressure	(0)	fixed Value	(0 0 0)	zeroGradient	(0)
atmosphere	pressureInletOutletVelocity	(0 0 0)	totalPressure	(0)	fixed Value	(0 0 0)	inletOutlet	(0)
WEC	movingWallVelocity	(0 0 0)	fixedFluxPressure	(0)	calculated	(0 0 0)	zeroGradient	(0)

Table 2

OpenFOAM solution schemes. See Ferziger et al. (2002); Versteeg and Malalasekera (2007) for details on the characteristics on the solution schemes.

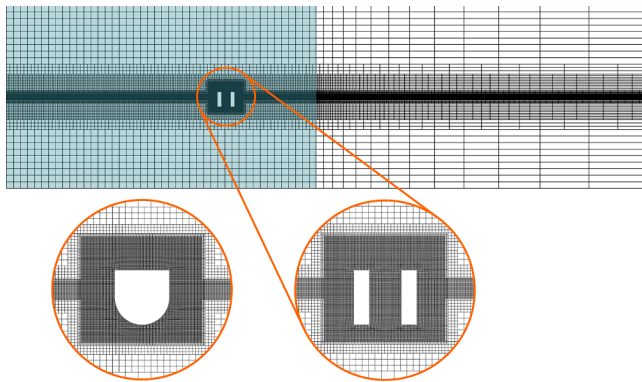|	Scheme	Order of accuracy
ddtSchemes	Euler	1st order
gradSchemes	Gauss linear	2nd order
laplacianSchemes	Gauss linear (corrected)	2nd order
divScheme U	Gauss total variation diminishing (TVD)	2nd order
divScheme α	Gauss TVD	2nd order

Fig. 8. Screen shot of the computational mesh in the xz-plane. The simulation zone, in which no cell grading is applied, is highlighted in blue. (For interpretation of the references to colour in this figure legend, the reader is referred to the web version of this article.)

(MULES) (Rusche, 2002).

The body motion, induced by the incident wave or external force, is solved via Newton's 2nd law of motion, within the *sixDoFRigidBodyMotionSolver* in the OpenFOAM framework. The motion solver provides a set of restraints, facilitating the numerical representation of linear PTO systems. The successful use of the motion solver to replicate a linear actuator type PTO system is demonstrated in (Penalba et al., 2018) and (Windt et al., 2020a). The resulting body motion is accommodated in the numerical domain through mesh morphing by means of the spherical linear interpolation (SLERP) algorithm.

Finally, based on (Windt et al., 2019b), laminar flow conditions are assumed for all simulations.

5.2. Numerical wave generation and absorption

The IHFOAM (Higuera et al., 2013) toolbox is employed for wave generation and absorption. IHFOAM is readily implemented in Open-FOAM v1812 and can be classified as a static boundary method (Windt et al., 2019c). Waves are generated at the up–wave boundary of the CFD–based NWT, by prescribing the target water level and the fluid velocity. For wave absorption, a correction velocity, based on shallow water theory, is imposed at the down–wave domain boundary, to cancel out the incoming wave.

5.3. Computational domain

The computational domain, as well as the solver setting and solution schemes, are adapted from Windt et al. (2019a). The CFD–based NWT spans a length of 21.1m (in the x–direction, see Figs. 7 (a) and (b)) and 7.8m in the y–direction, perpendicular to the wave propagation direction. In the z–direction, the CFD–based NWT spans 6m, and the water depth is set to 3m. The still water line is located at $z = 0$. The structure is located 7.2m down–wave from the wave generation boundary, and 13.9m up–wave from the absorption boundary, corresponding to $(x,y,z) = (0,0,0)$.

The symmetry of the problem is exploited, and a symmetry boundary condition is applied in the xz-plane, at $y = 0$ (see Fig. 7 (b)).

5.3.1. Boundary conditions and solution schemes

The OpenFOAM specific boundary conditions for all domain boundaries (according to Fig. 7) are listed in Table 1. The OpenFOAM specific solution schemes for the temporal derivatives, gradients, divergence and the Laplace equation are listed in Table 2.

5.3.2. Discretisation

To determine the converged spatial and temporal discretisation size, *i.e.* time step and cell size, comprehensive convergence studies have been performed by Windt et al. (2019a, 2020b, 2020c), based on which a fixed time step of $\Delta t = 0.002s$ is used together with a minimum spatial discretisation size of 10 cells per significant wave height H_s (i.e., $0.01m$) in the phase interface region and in the vicinity of the WEC structure in the z–direction. Within the simulation zone (see Fig. 8), a maximum aspect ratio of 2 and 4 is used in the x– and y–directions, respectively. A screen shot of the spatial discretisation is depicted in Fig. 8. The overall cell count in the domain is 6.9M and 6.7M for WEC structure W1 and W2, respectively. The employed discretisation yields typical maximum y^+ values of the order of $\mathcal{O}(300)$ and $\mathcal{O}(100)$ for WEC structure W1 and W2, respectively.

6. Results and discussion

This section presents and discusses the results of the three different steps: System identification and control design, validation, and controller evaluation.

6.1. System identification and control design

Using the data generated with the CFD–based NWT, *i.e.* the set of chirp inputs $\mathcal{U} = \{f_i\}_{i=1}^3$, and their corresponding outputs (velocities) $\mathcal{Y} = \{y_i\}_{i=1}^3$ (see Fig. 9), the system identification procedure, described in Section 3.1, can be readily considered, to compute a mathematical (parametric) representation for each WEC system W1 and W2. In particular, two 8th-order[6] nominal linear models, Σ_1 and Σ_2 (as in Equation (3)), are obtained for the force–to–velocity mappings associated with W1 and W2, respectively. The frequency responses of Σ_1 and

---

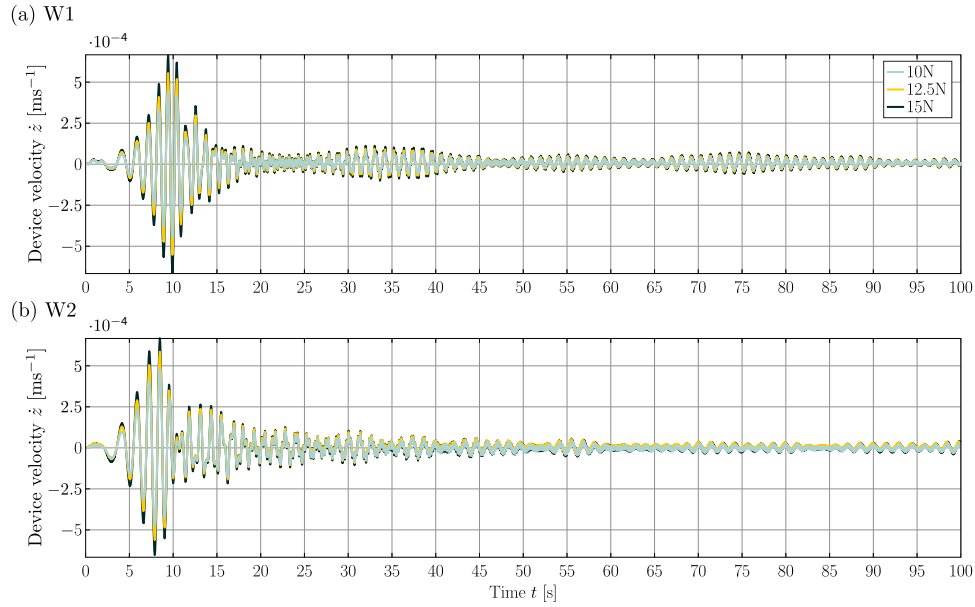[6] The expression '8th-order' refers to $n = 8$ in Equation (3).

Fig. 9. Time traces of the WEC velocity $\dot{z}$ of W1 (a) and W2 (b), for the multi–frequency (chirp) forced oscillation test.
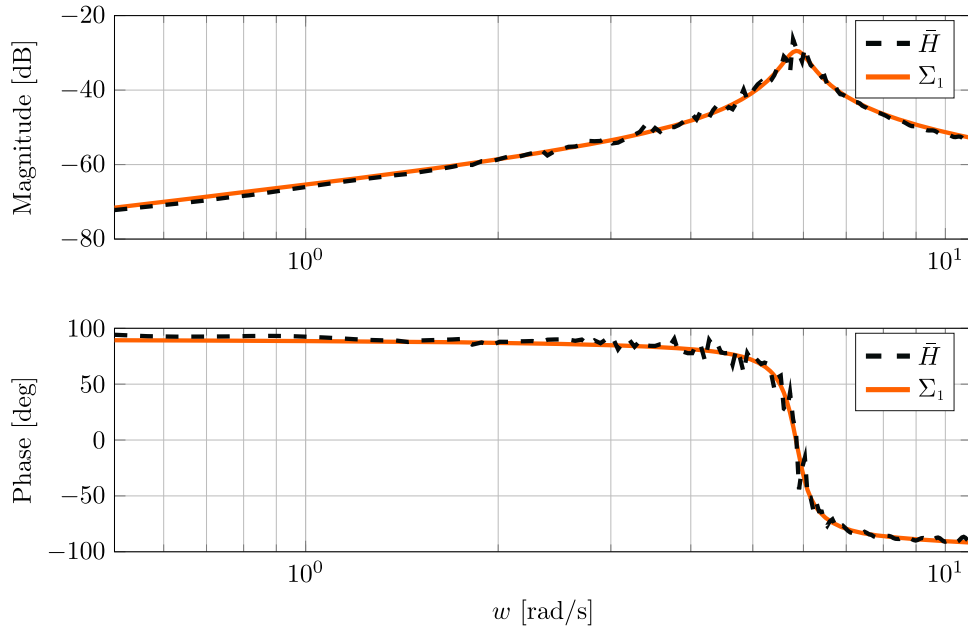

Fig. 10. Bode plot for the force-to-velocity frequency response associated with geometry W1, including the average ETFE $\bar{H}$ and the approximating system Σ_1.

Σ_2, along with each corresponding average ETFE $\bar{H}$ (see Equation (2)), are shown in the Bode plots of Figs. 10 and 11, respectively.

With the identified linear WEC model, the three EMCSs are synthesised under the assumption of perfect knowledge of the wave excitation force. For the sake of completeness, Fig. 12 shows the resulting wave excitation force on WEC structures W1 and W2 from the wave excitation force tests. Optimal control parameters (stiffness and damping) for the feedback controllers (see Table 3), as well as optimal control force time traces for the feedforward (moment-based) controller (see Fig. 13) are now determined based on the identified control design models. Note that the peak frequency associated with the stochastic description of the input is $\omega_p = 2\pi \cdot 1.94s \approx 3.3rads^{-1}$, which is significantly distant from the frequency range containing the device resonant dynamics. This inherently implies that a substantial control effort (i.e., large PTO force amplitudes) will be required to drive both geometries

W1 and W2 towards resonance with the input wave (Ringwood et al., 2019).

6.2. Validation

To ensure and assess the quality of the identified linear WEC models, simulations under *uncontrolled* conditions are performed in the CFD–based and linear modelling framework.

6.2.1. W1

Fig. 14 shows the time traces of the WEC displacement (a) and velocity (b) for W1 for the case of an uncontrolled device from the CFD–based and linear modelling framework. Excellent agreement between the different models is achieved with a normalised root–mean square deviation (nRMSD), following Equation (16), of 1.4% and 1.6%
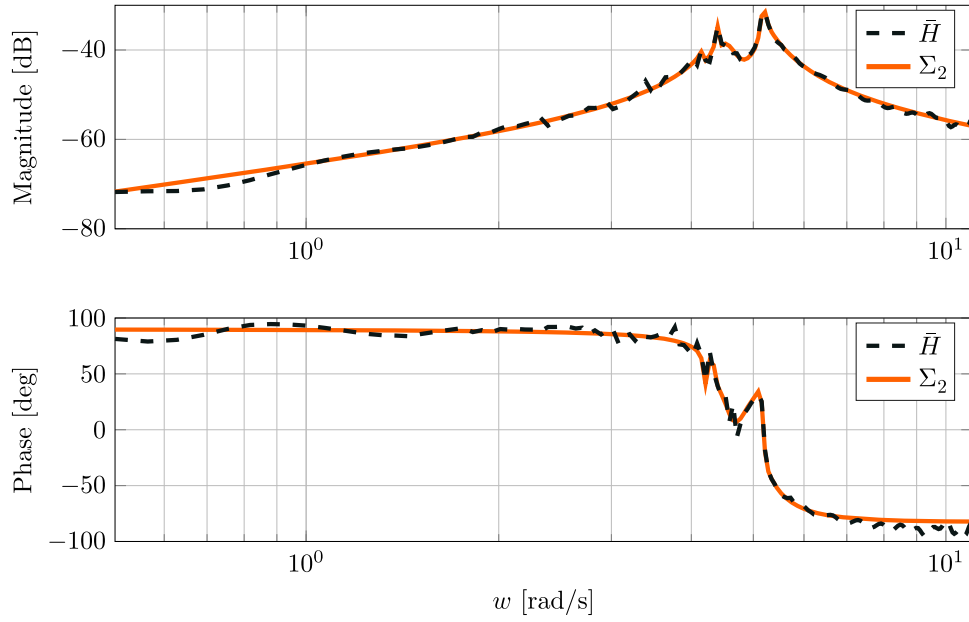
Fig. 11. Bode plot for the force-to-velocity frequency response associated with geometry W2, comparing the average ETFE $\bar{H}$ and the approximating system Σ_2.
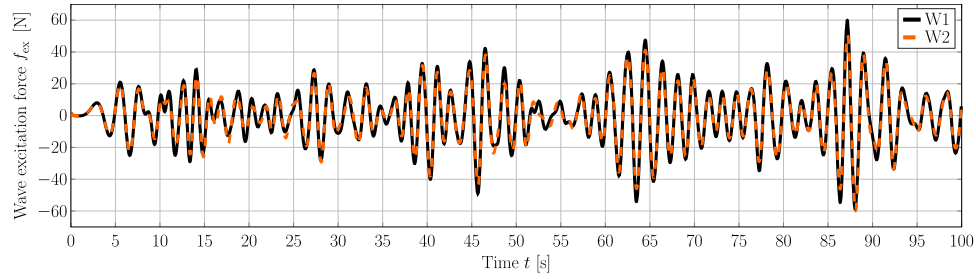

Fig. 12. Time trace of the wave excitation force on the fixed WEC structures W1 (a) and W2 (b).

Table 3
Optimal stiffness and damping coefficients of the reactive feedback controller for W1 and W2.

	Reactive		Resistive
	K_1 [Nm^{-1}]	B_1 [Nsm^{-1}]	B_2 [Nsm^{-1}]
W1	-1318	64	23
W2	-1385	33	59

for the device displacement and velocity, respectively.

$$\mathrm{nRMSD} = \sqrt{\frac{\sum_{i=1}^{n}[y_{\mathrm{CFD}}(i) - y_{\mathrm{Lin}}(i)]^2}{n}} \; \frac{100\%}{\mathscr{N}} \tag{16}$$

In Equation (16), y_{CFD} denotes the quantity from the CFD–based NWT, y_{Lin} is the corresponding quantity from the linear model, and n defines the signal length via the number of samples. Normalisation is achieved by $\mathscr{N} = \max(y_{\mathrm{CFD}}) + |\min(y_{\mathrm{CFD}})|$.

6.2.2. W2

Fig. 15 shows the time traces of the WEC displacement (a) and velocity (b) for W2 for the case of an uncontrolled device from the
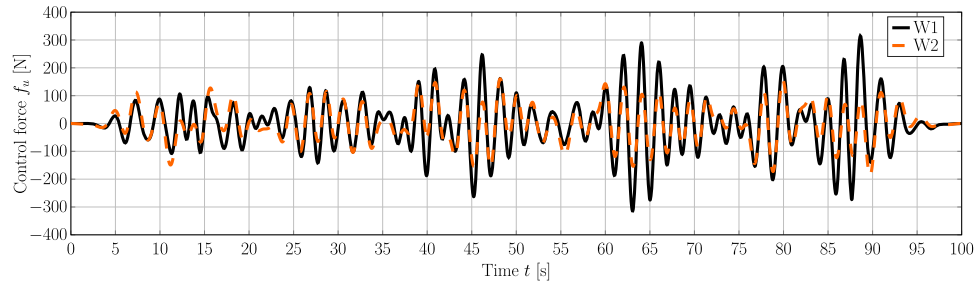

Fig. 13. Time trace of the control force f_u for the feedforward controller for WEC structures W1 and W2.
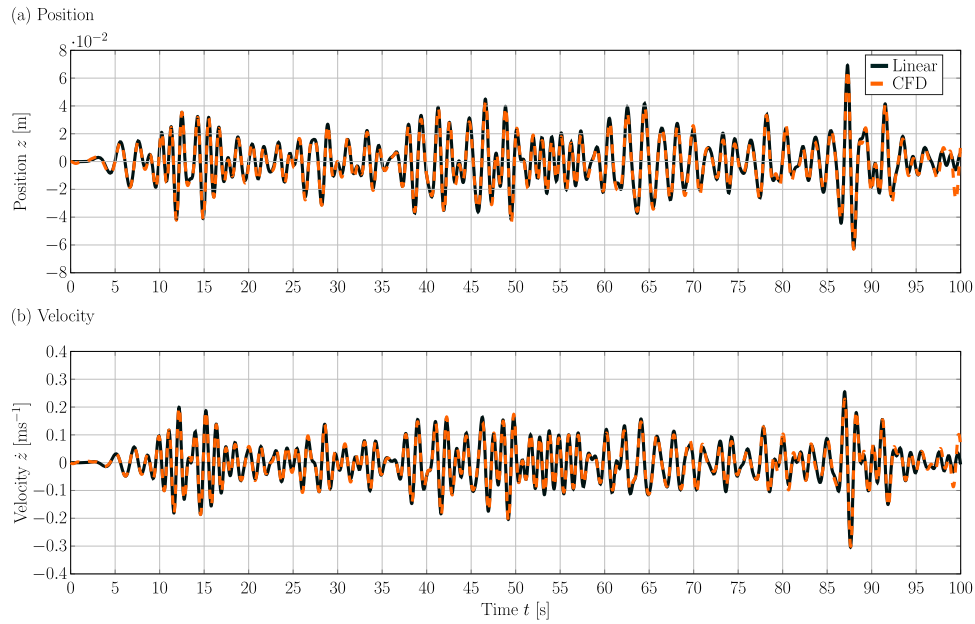
(a) Position

(b) Velocity

Fig. 14. Time traces of the WEC displacement (a) and velocity (b) for W1.

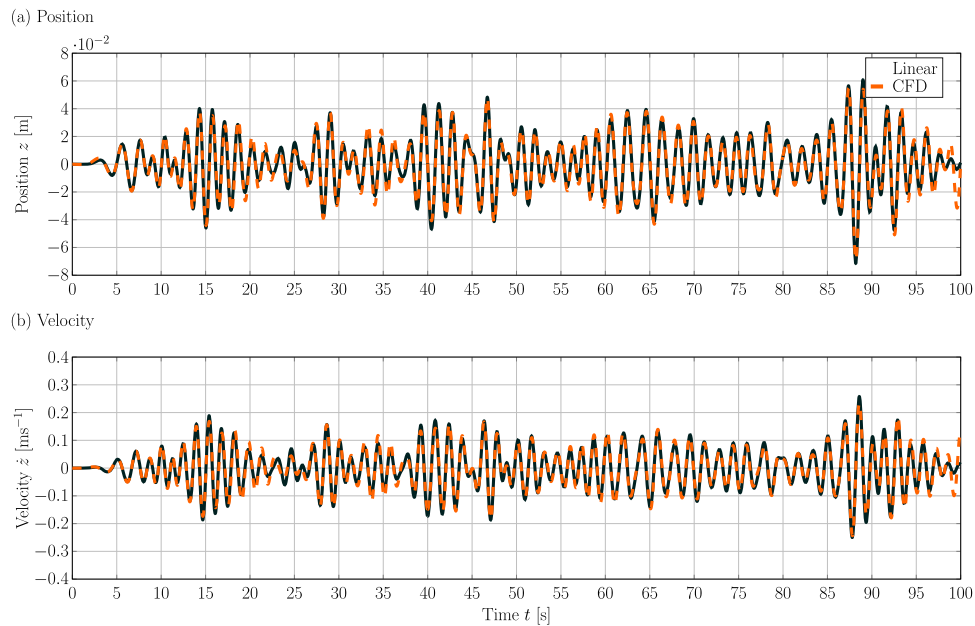(a) Position

(b) Velocity

Fig. 15. Time trace of the WEC displacement (a) and velocity (b) for W2.

CFD–based and linear modelling framework. As in the case for W1, excellent agreement between the different models is achieved with a normalised root–mean square deviation (nRMSD) of 2.4% and 2.7% for the device displacement and velocity, respectively.

Overall, the results of the validation step highlight the accuracy of the identified, linear WEC models (under the specified uncontrolled conditions), thereby forming the basis of a fair comparison in the subsequent controller evaluation step.

6.3. Performance evaluation

In the performance evaluation step, the results of the device displacement z and velocity $\dot{z}$ data, as well as the control force f_u and the instantaneous power, P, are compared between the CFD–based and the linear modelling framework. Furthermore, the cumulative absorbed energy, $\mathscr{E}$, and the deviation rate of the absorbed energy, $\mathscr{D}$, following Equation (17), are compared.

$$\mathscr{D} = \left(1 - \frac{E_{\mathrm{CFD}}}{E_{\mathrm{Lin}}}\right) \cdot 100\% , \tag{17}$$

where E_{CFD} follows:

$$E_{\mathrm{CFD}} = \frac{1}{t_{\mathrm{sim}}} \int_{t_{\mathrm{sim}}} P_{\mathrm{CFD}} \, \mathrm{d}t_{\mathrm{sim}} , \tag{18}$$

and

$$E_{\mathrm{Lin}} = \frac{1}{t_{\mathrm{sim}}} \int_{t_{\mathrm{sim}}} P_{\mathrm{Lin}} \, \mathrm{d}t_{\mathrm{sim}} , \tag{19}$$

where t_{sim} (=100s) is the simulated time. Consequently, a deviation rate
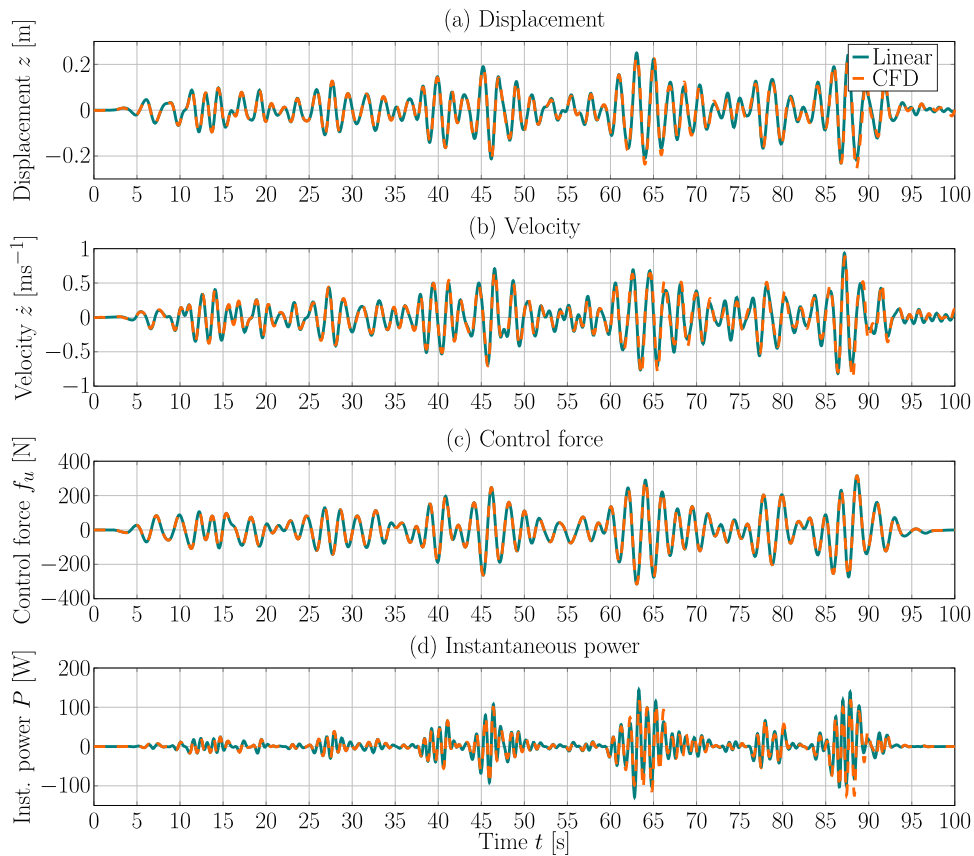
Fig. 16. Time trace of the device displacement (a), velocity (b), control force (c), and instantaneous power (d) for W1 with the feedforward controller.

$> 0\%$ indicates an over–prediction of the absorbed energy with the linear WEC model, thereby highlighting the WEC modelling paradox.

6.3.1. W1

Figs. 16, 17, and 18 show the time traces of the device displacement and velocity data, the control force, and the instantaneous power of W1 for the three different EMCSs: feedforward, reactive feedback, and resistive feedback, respectively. It can readily be seen that all the relevant quantities follow the same trend, whereby more aggressive controllers increase the magnitude of displacement, velocity, control force, and instantaneous power. Furthermore, it can clearly be seen that the feedforward and reactive feedback EMCS generate, at times, negative instantaneous power, which is a characteristic of reactive control. The instantaneous power for the resistive feedback controller is continuously positive.

For the quantitative assessment of the difference between the linear and CFD–based model predictions for the different EMCSs, Table 4 lists the nRMSD (following Equation (16)) for the device displacement and velocity, the control force, and the instantaneous power. Table 4 also contains the values of $\mathscr{D}$.

For the resistive feedback controller, relatively small values, of the order of 2%, are computed for the nRMSDs for the displacement, velocity, control force, and instantaneous power, indicating relatively linear device behaviour. These values of the nRMSDs increase relative consistently (to ∼ 5%) for all the considered data for the reactive feedback controller. The increased nRMSDs suggest a stronger influence of hydrodynamic non–linearities due to the enhanced WEC motion. Interestingly, for the most aggressive controller in this study, the feedforward EMCS, the nRMSDs lie between the calculated values for the resistive and reactive feedback controller (∼ 3%). Note that the nRMSD for the control force is 0% since the exact same control force is applied to the system in the linear and CFD–based modelling framework. The

higher nRMSE for the reactive feedback controller, compared to the feedforward controller, is explained by the significantly greater *system sensitivity* (the sensitivity of the closed-loop response to modelling errors) for reactive feedback controllers (see Ringwood et al., 2019). However, as documented in Ringwood et al. (2019), it is not always the case that a large system (closed-loop) sensitivity transfers into power production sensitivity to modelling errors. This indeed, is the case for the power production results shown in Table 2, where the feedforward controller demonstrated a greater sensitivity in power production to modelling errors than the feedback controller, consistent with the predictions in Ringwood et al. (2019). This can be explained by the fact that while feedback control structures are capable of modifying the internal dynamics of the WEC in real-time according to the control objective, *i.e.* using actual measurements from the CFD numerical wave tank, the feedforward controller is implemented in terms of an open-loop control law, so that no information on the actual displacement/position of the device is involved in its computation. In addition to poorer power production sensitivity properties, the feedforward controller also has more aggressive control actions, which are likely to be an additional trigger of nonlinear effects, directly impacting the quality of the (linear) control solution in terms of energy absorption, *i.e.* having a direct negative influence in $\mathscr{D}$.

Regarding $\mathscr{D}$, for the resistive case, the realistic performance of the EMCS in the CFD–based model, by means of the absorbed energy, is evaluated to be 98.3% of the predicted performance from the linear hydrodynamic model (i.e. $\mathscr{D} = 1.7\%$). For the reactive feedback controller $\mathscr{D} = 5.2\%$, again indicating that the accuracy of the linear model deteriorates under more aggressive control action. The trend of $\mathscr{D}$ is consistent with the findings for the nRMSDs and is indirectly visualised in Fig. 19, showing the time trace of the cumulative absorbed energy. Finally, for the reactive feedforward controller, a deviation rate of 22.4% is calculated, thereby following the trend of reduced accuracy
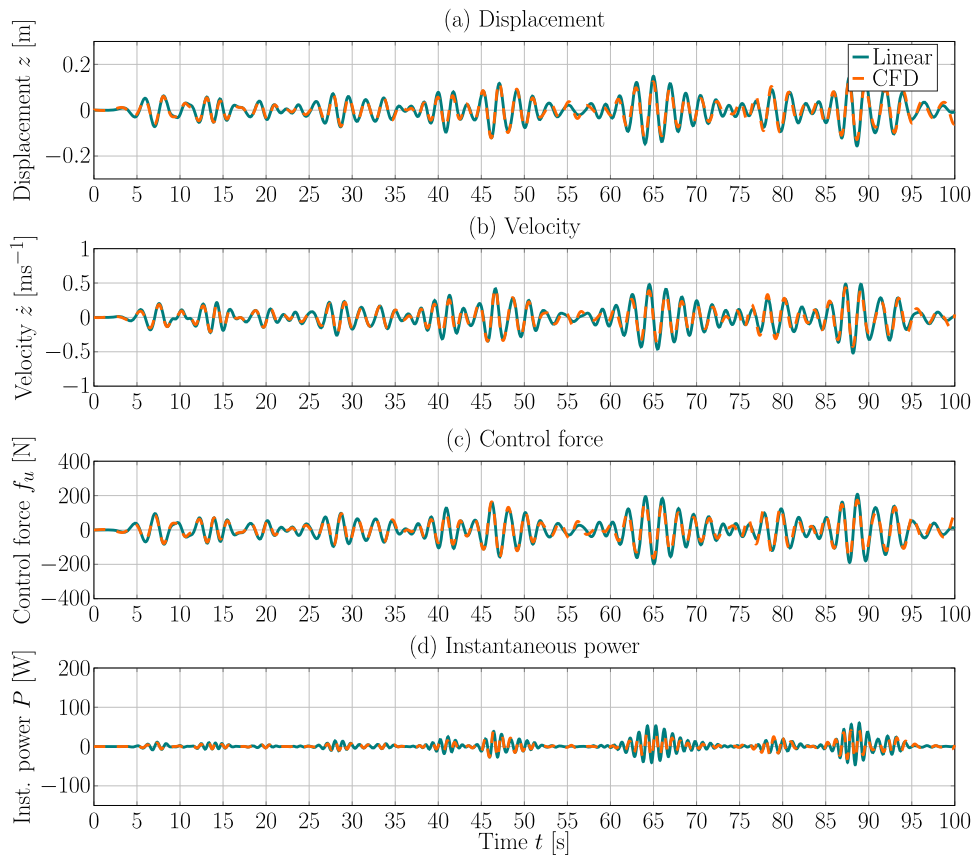
Fig. 17. Time trace of the device displacement (a), velocity (b), control force (c), and instantaneous power (d) for W1 with the reactive feedback controller.

of the linear model under increased control action. Again, the observed deviation between the linear and the CFD–based model is clearly visualised in Fig. 19. However, as stated in the previous paragraph, relatively small values of the nRMSDs are calculated for the feedforward controller.

By way of example, Fig. 20 shows a close up of the time traces in Fig. 16, between 58s and 72s. In this time window, relatively large (compared to the preceding and succeeding part of the time trace) deviation in the device velocity between the linear and CFD–based model can be observed, specifically with respect to the instantaneous phase synchronisation between signals, which is known to be a key factor in the energy-maximising optimality principle (Falnes, 2002). Given that the control force is the same in both models, the deviations in the velocity are the sole cause for the deviations in the instantaneous power. Even though the deviations in the instantaneous power appear, qualitatively, to be relatively moderate (as suggested by the nRMSD), cumulatively, such deviations have, as shown here, a potentially significant influence on the performance assessment of EMCSs. Thus, the results for the reactive feedforward controller highlight the importance of a complete analysis of all data influencing the performance assessment of an EMCS.

6.3.2. W2

For W2, the values of the nRMSD for the device displacement, velocity, control force, and instantaneous power, as well as the cumulative absorbed energy, and the deviation rate of the absorbed energy follow the same trend as previously observed for W1. Table 5 lists the nRMSDs

of the relevant quantities between the linear and CFD–based model for the three different EMCSs, as well as the deviation rate of the absorbed energy. Fig. 21 shows the corresponding time traces of the cumulative absorbed energy.

For the resistive feedback controller, the values of the nRMSDs, as well as $\mathscr{D}$, are almost identical, compared with W1, highlighting the linearity of this case even when a structure whose geometry, *i.e.* sharp edges, is likely to induce non–linear hydrodynamic effects, such as vortex shedding, are considered. The effects of geometry–induced non-–linearities are clearly highlighted by the deviation rate of the absorbed energy $\mathscr{D}$ for the cases of more aggressive control action. For the case of the reactive feedback controller, only 57.4% of the absorbed energy, predicted by the linear model, are absorbed in the CFD–model (i.e. $\mathscr{D} = $ 42.6%). An even further reduction ($\mathscr{D} = $ 52.8%) can be calculated for the feedforward controller. Given the similarity of the test cases (*i.e.* incident sea state), the structural dimensions, and the excellent validation of the linear model under uncontrolled conditions for both WEC structures, the observed effects can be confidently put down to shape-–induced non–linearities.

7. Conclusions

The present paper investigates the influence of different modelling frameworks (linear and CFD–based) on the performance assessment of EMCSs. Considering three different controllers of varying aggressiveness, implemented in two different WEC structures, the presented results allow a comprehensive assessment of the effects of the
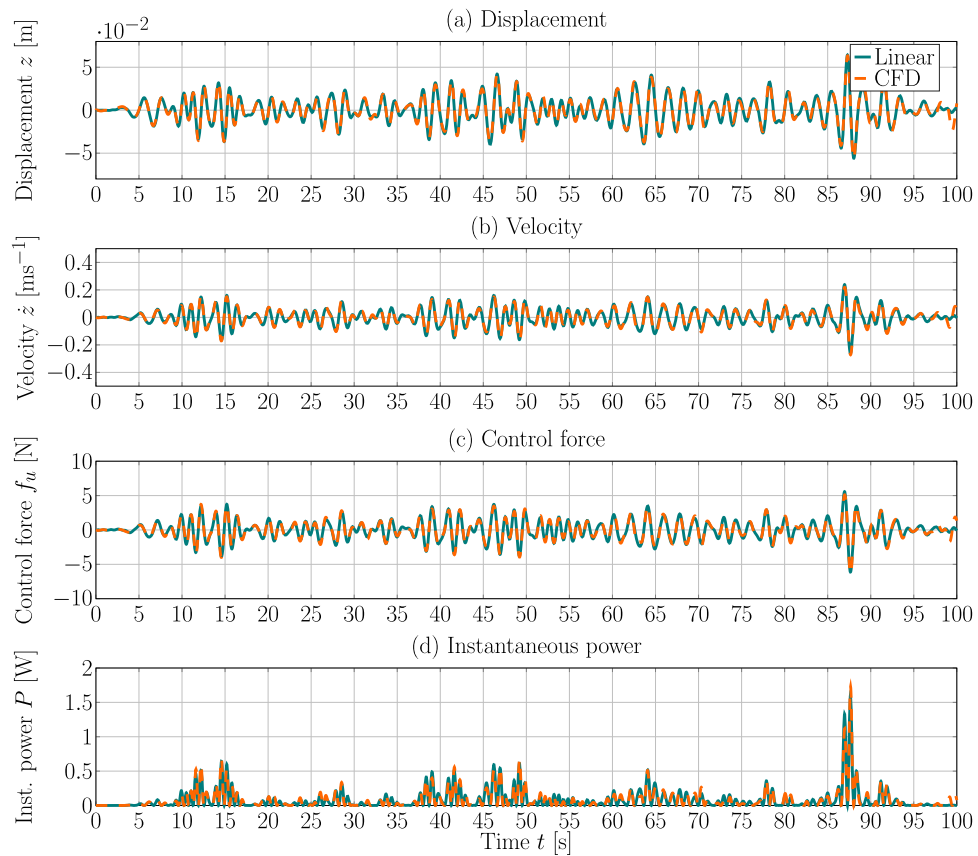
Fig. 18. Time trace of the device displacement (a), velocity (b), control force (c), and instantaneous power (d) for W1 with the resistive feedback controller.

Table 4
Deviation between the linear and CFD model for the controller evaluation of W1.

	Feedback Resistive	Feedback Reactive	Feedforward
Displacement z	1.4%	5.0%	2.1%
Velocity $\dot{z}$	1.8%	5.2%	2.8%
Control force f_u	1.8%	5.0%	0%
Instantaneous power P	1.7%	6.3%	3.0%
$\mathscr{D}$	1.7%	5.2%	22.4%

fidelity–imbalance between the design and evaluation framework of EMCSs.

The paper aims at answering the question if linear reactive controller are limited by inherently violating the underlying assumptions within the (linear) design model through the control objective function. Based on the results the answer to this question is: Yes, linear reactive controllers are, for linear models obtained by exciting the WEC with small amplitude signals, inherently limited by the WEC modelling paradox, such that power production estimation is significantly over–predicted by the control design model when more aggressive controllers are employed. Since linear models will likely be the first choice during control design, it is important to evaluate the performance of the designed controller under realistic, non–linear conditions.

It should be noted that the validation of the identified linear model and power production assessment have been performed using relatively linear wave excitation, in order to show the effect of EMCS on the performance of the linear model. If more non–linear wave excitation is considered, larger errors in the identified linear model can be expected.

Finally, note that the linear hydrodynamic models used within this study are based on system identification, thereby are likely to be more
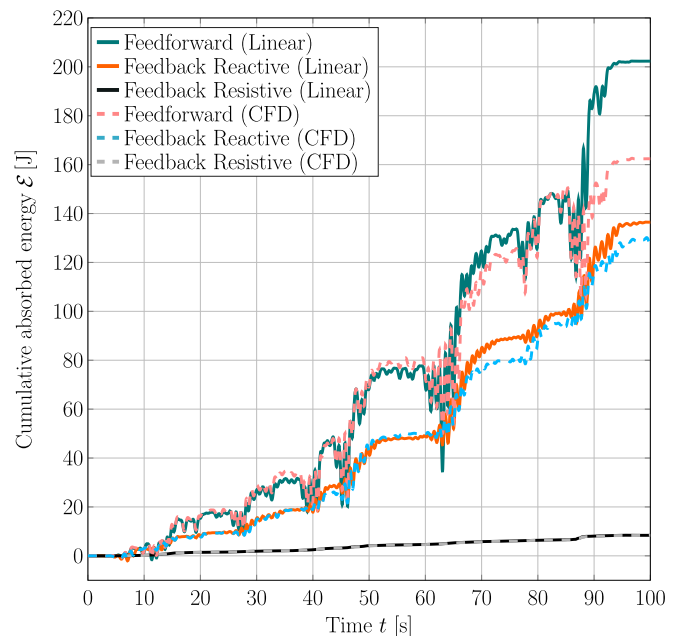

Fig. 19. Time trace of the cumulative absorbed energy for W1 with the three different EMCSs.

representative of the average system dynamics (Davidson et al., 2015) compared to linear models based on BEM–based potential flow solutions. Hence, the deterioration in the performance of BEM–based models compared to CFD–based models may be even more severe than the deterioration observed in this study. Thus, for controllers designed on
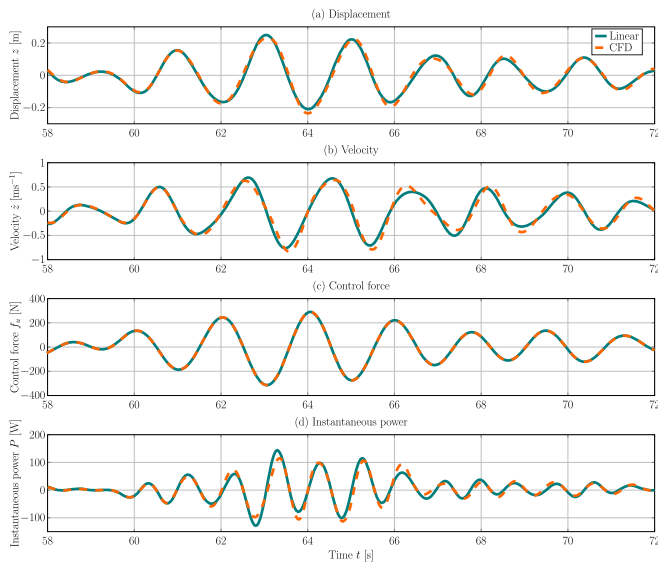
Fig. 20. Close up of the time trace of the device displacement (a), velocity (b), control force (c), and instantaneous power (d) for W1 with the feedforward controller.

Table 5
Deviation between the linear and CFD–based model for the controller evaluation of W2.

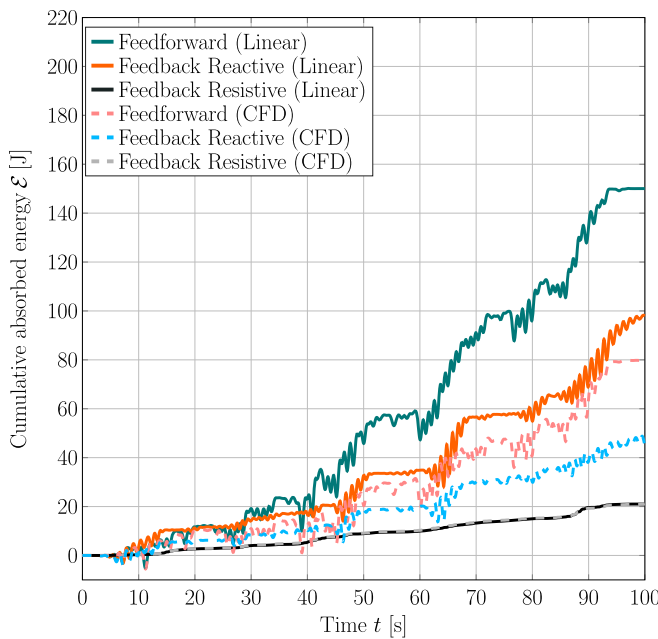|	Feedback Resistive	Feedback Reactive	Feedforward
displacement z	1.6%	5.7%	2.7%
Velocity $\dot{z}$	1.8%	5.4%	3.7%
Control force f_u	1.9%	5.7%	0%
Instantaneous power P	2.6%	6.9%	3.1%
$\mathscr{D}$	1.9%	42.6%	52.8%

Fig. 21. Time trace of the cumulative absorbed energy for W2 with the three different EMCSs.

BEM–based models, a rigorous evaluation of the performance under realistic conditions is vital.

Declaration of Competing Interest

The authors declare no conflict of interest. The founding sponsors had no role in the design of the study; in the collection, analyses, or interpretation of data; in the writing of the manuscript, and in the decision to publish the results.

Acknowledgment

References

Astolfi, A., 2010. Model reduction by moment matching for linear and nonlinear systems. IEEE Trans. Automat. Contr. 55 (10), 2321–2336.

Bacelli, G., Coe, R.G., Patterson, D., Wilson, D., 2017. System identification of a heaving point absorber: design of experiment and device modeling. Energies 10 (4), 472.

Berberović, E., van Hinsberg, N.P., Jakirlić, S., Roisman, I.V., Tropea, C., 2009. Drop impact onto a liquid layer of finite thickness: Dynamics of the cavity evolution. Physical Review E 79.036306–1 – 036306–15

Brewer, J., 1978. Kronecker products and matrix calculus in system theory. IEEE Transactions on Circuits and Systems 25 (9), 772–781.

Davidson, J., Genest, R., Ringwood, J.V., 2018. Adaptive control of a wave energy converter. IEEE Trans. Sustainable Energy 9 (4), 1588–1595.

Davidson, J., Giorgi, S., Ringwood, J.V., 2015. Linear parametric hydrodynamic models for ocean wave energy converters identified from numerical wave tank experiments. Ocean Eng. 103, 31–39.

Davidson, J., Giorgi, S., Ringwood, J.V., 2016. Identification of wave energy device models from numerical wave tank data—part 1: numerical wave tank identification tests. IEEE Trans. Sustainable Energy 7 (3), 1012–1019.

Davidson, J., Windt, C., Giorgi, G., Genest, R., Ringwood, J., 2017. Evaluation of Energy Maximising Control Systems for Wave Energy Converters Using OpenFOAM. Selected papers of the 11th OpenFOAM Workshop. Springer International Publishing AG.

Faedo, N., 2020. Optimal control and model reduction for wave energy systems: A moment-based approach (PhD Thesis). Department of Electronic Engineering, Maynooth University.

Faedo, N., Olaya, S., Ringwood, J.V., 2017. Optimal control, MPC and MPC-like algorithms for wave energy systems: an overview. IFAC Journal of Systems and Control 1, 37–56.

Faedo, N., Pena-Sanchez, Y., Ringwood, J., 2020. Receding-horizon energy-maximising optimal control of wave energy systems based on moments. IEEE Trans. Sustainable Energy.

Faedo, N., Peña-Sanchez, Y., Ringwood, J.V., 2018. Finite-order hydrodynamic model determination for wave energy applications using moment-matching. Ocean Eng. 163, 251–263.

Faedo, N., Peña-Sanchez, Y., Ringwood, J.V., 2018. Passivity preserving moment-based finite-order hydrodynamic model identification for wave energy applications. Proceedings of the 3rd International Conference on Renewable Energies Offshore (RENEW), Lisbon, Portugal, pp. 351–359.

Faedo, N., Scarciotti, G., Astolfi, A., Ringwood, J.V., 2018. Energy-maximising control of wave energy converters using a moment-domain representation. Control Eng. Pract. 81, 85–96.

Faedo, N., Scarciotti, G., Astolfi, A., Ringwood, J.V., 2019. Moment-based constrained optimal control of an array of wave energy converters. 2019 American Control Conference (ACC), Philadelphia, pp. 4797–4802.

Falnes, J., 2002. Ocean waves and oscillating systems: Linear interactions including wave-energy extraction. Cambridge University Press.

Ferziger, J.H., Perić, M., Street, R.L., 2002. Computational methods for fluid dynamics, 3. Springer.

Giorgi, G., Ringwood, J.V., 2016. Implementation of latching control in a numerical wave tank with regular waves. Journal of Ocean Engineering and Marine Energy 2, 211–226.

Heller, V., 2011. Scale effects in physical hydraulic engineering models. Journal of Hydraulic Research 49 (3), 293–306.

Higuera, P., Lara, J.L., Losada, I.J., 2013. Simulating coastal engineering processes with OpenFOAM. Coastal Eng. 71, 119–134.

Hirt, C.W., Nichols, B.D., 1981. Volume of fluid (VOF) method for the dynamics of free boundaries. J. Comput. Phys. 39, 201–225.

Isidori, A., 2013. Nonlinear control systems. Springer Science & Business Media.

Khalil, H.K., 1996. Noninear systems. Prentice-Hall, New Jersey.

Kim, C.H., Clement, A.H., Tanizawa, K., 1999. Recent research and development of numerical wave tanks – a review. Int. J. Offshore Polar Eng. 9 (4), 1–16.

Kim, J.W., Jang, H., Baquet, A., O'Sullivan, J., Lee, S., Kim, B., Jasak, H., 2016. Technical and economic readiness review of CFD-based numerical wave basin for offshore floater design. Proceedings of the Offshore Technology Conference, Houston, TX, USA.

Ljung, L., 1999. System identification - Theory for the user. Prentice Hall.

Penalba, M., Davidson, J., Windt, C., Ringwood, J.V., 2018. A high-fidelity wave-to-wire simulation platform for wave energy converters: coupled numerical wave tank and power take-off models. Appl. Energy 226, 655–669.

Penalba, M., Ringwood, J.V., 2019. Linearisation-based nonlinearity measures for wave-to-wire models in wave energy. Ocean Eng. 171, 496–504.

Penalba, M., Ringwood, J.V., 2020. Systematic complexity reduction of wave-to-wire models for wave energy system design. Ocean Eng. 217, 107651.

Ransley, E., Brown, S., Hann, M., Greaves, D., Windt, C., Ringwood, J., Davidson, J., Schmitt, P., Yan, S., Wang, J.X., Wang, J.H., Ma, Q., Xie, Z., Giorgi, G., Hughes, J., Williams, A., Masters, I., Lin, Z., Chen, H., Qian, L., Ma, Z., Chen, Q., Ding, H., Zang, J., van Rij, J., Yu, Y., Li, Z., Bouscasse, B., Ducrozet, G., Bingham, H., 2020a. Focused wave interactions with floating structures: A blind comparative study. Proceedings of the Institution of Civil Engineers - Engineering and Computational Mechanics 1–16.

Ransley, E., Yan, S., Brown, S., Hann, M., Graham, D., Windt, C., Schmitt, P., Davidson, J., Ringwood, J., Musiedlak, P.-H., Wang, J., Wang, J., Ma, Q., Xie, Z., Zhang, N., Zheng, X., Giorgi, G., Chen, H., Lin, Z., Qian, L., Ma, Z., Bai, W., Chen, Q., Zang, J., Ding, H., Cheng, L., Zheng, J., Gu, H., Gong, X., Liu, Z., Zhuang, Y., Wan, D., Bingham, H., Greaves, D., 2020b. A blind comparative study of focused wave interactions with floating structures (CCP-WSI blind test series 3). Int. J. Offshore Polar Eng. 30 (1), 1–10.

Ringwood, J.V., Bacelli, G., Fusco, F., 2014. Energy-maximizing control of wave-energy converters: the development of control system technology to optimize their operation. IEEE Control Syst. 34, 30–55.

Ringwood, J.V., Mérigaud, A., Faedo, N., Fusco, F., 2019. An analytical and numerical sensitivity and robustness analysis of wave energy control systems. IEEE Trans. Control Syst. Technol.

Rusche, H., 2002. Computational fluid dynamics of dispersed two-phase flows at high phase fractions (PhD Thesis). Department of Mechanical Engineering, Imperial College London.

Sharkey, F., Bannon, E., Conlon, M., Gaughan, K., 2011. Dynamic electrical ratings and the economics of capacity factor for wave energy converter arrays. Proceedings of the 9th European Wave and Tidal Energy Conference, Southampton, UK.

Tanizawa, K., Naito, S., 1997. A study on parametric roll motions by fully nonlinear numerical wave tank. Proceedings of the 7th International Offshore and Polar Engineering Conference, Honolulu, HI, USA.

Versteeg, H.K., Malalasekera, W., 2007. An introduction to computational fluid dynamics: The finite volume method. Pearson education.

Wei, Y., Rafiee, A., Henry, A., Dias, F., 2015. Wave interaction with an oscillating wave surge converter, part I: Viscous effects. Ocean Eng. 104, 185–203.

Windt, C., Davidson, J., Chandar, D.D., Faedo, N., Ringwood, J.V., 2019. Evaluation of the overset grid method for control studies of wave energy converters in openfoam numerical wave tanks. Journal of Ocean Engineering and Marine Energy 1–16.

Windt, C., Davidson, J., Ransley, E.J., Greaves, D., Jakobsen, M., Kramer, M., Ringwood, J.V., 2020. Validation of a CFD-based numerical wave tank model for the power production assessment of the wavestar ocean wave energy converter. Renew. Energy 146, 2499–2516.

Windt, C., Davidson, J., Ringwood, J., 2018. High-fidelity numerical modelling of ocean wave energy systems: A review of computational fluid dynamics-based numerical wave tanks. Renewable Sustainable Energy Rev. 93, 610–630.

Windt, C., Davidson, J., Schmitt, P., Ringwood, J., 2020. Wave–structure interaction of wave energy converters: a sensitivity analysis. Proceedings of the Institution of Civil Engineers - Engineering and Computational Mechanics accepted for publication.

Windt, C., Davidson, J., Schmitt, P., Ringwood, J.V., 2019. Contribution to the CCP-WSI blind test series 2: CFD-based numerical wave tank experiments employing an impulse source wave maker. Proceedings of the 13th European Wave and Tidal Energy Conference (EWTEC), Naples, Italy.

Windt, C., Davidson, J., Schmitt, P., Ringwood, J.V., 2019. On the assessment of numerical wave makers for CFD simulations. J. Mar. Sci. Eng. 7 (2), 47.

Windt, C., Faedo, N., Penalba, M., Ringwood, J., 2018. Evaluation of energy maximising control systems for the wavestar wave energy converter. Proceedings of the 2019 American Control Conference, Philadelphia, USA.

Windt, C., Ringwood, J.V., Davidson, J., Schmitt, P., et al., 2020. CCP-WSI Blind test series 3: CFD-based numerical wave tank experiments employing an impulse source wave maker. Int. J. Offshore Polar Eng. 30 (01), 28–35.